

# Hybrid Organic-Inorganic Halides $(C_5H_7N_2)_2MBr_4$ ( $M = Hg, Zn$ ) with High Color Rendering Index and High Efficiency White-Light Emission

Aymen Yangui,<sup>1,‡</sup> Rachel Rocanova,<sup>1,‡</sup> Timothy M. McWhorter,<sup>1</sup> Yuntao Wu,<sup>2</sup> Mao-Hua Du,<sup>3,\*</sup> and Bayrammurad Saparov<sup>1,\*</sup>

<sup>1</sup>Department of Chemistry and Biochemistry, University of Oklahoma, 101 Stephenson Parkway, Norman, OK 73019, USA

<sup>2</sup>Department of Materials Science and Engineering, University of Tennessee, Knoxville, TN 37996, USA

<sup>3</sup>Materials Science and Technology Division, Oak Ridge National Laboratory, Oak Ridge, TN 37831, USA

<sup>‡</sup>These two authors contributed equally to this work.

**ABSTRACT:** Low-dimensional hybrid organic-inorganic materials (HOIMs) are being widely investigated for their unique optoelectronic properties. Some of them exhibit broadband white-light (WL) emission upon UV excitation, providing a potential for the fabrication of single-component white-light emitting diodes (WLEDs). Here, we report new examples of low-dimensional HOIMs, based on 4-aminopyridine (4AMP) and group 12 metals (Hg and Zn), for single-component WL emission. The 4AMP cation containing structures feature  $HgBr_4$  and  $ZnBr_4$  isolated tetrahedra in  $(C_5H_7N_2)_2HgBr_4 \cdot H_2O$  (**1**) and  $(C_5H_7N_2)_2ZnBr_4$  (**2**), respectively. The presence of discrete molecular building blocks in the zero-dimensional (0D) structures result in strongly localized charges and bright WL luminescence with a corresponding Commission Internationale de l'Eclairage (CIE) Color Coordinates of (0.34, 0.38) and (0.25, 0.26), correlated color temperatures (CCT) of 5206 K (**1**) and 11630 K (**2**) and very high color rendering index (CRI) of 87 (**1**) and 96 (**2**). The visibly bright WL emission at room temperature is corroborated with high measured photoluminescence quantum yield (PLQY) values of 14.87 and 19.18% for **1** and **2**, respectively. Notably, the measured high CRI values for these new HOIMs exceed the commercial requirements and affords both “warm” and “cold” WL depending on the metal used (Hg or Zn). Based on temperature- and powder-dependent photoluminescence (PL), PL lifetimes measurements and density functional theory (DFT) calculations, the broadband WL emission is assigned to the 4AMP organic molecules emission and self-trapped states.

## INTRODUCTION

According to the U.S. Energy Information Administration, 21% of all energy consumed in the U.S. in 2017 was from lighting. By replacing incandescent bulbs with light-emitting diodes (LEDs), 40% power consumption reduction is projected to be achieved by 2030.<sup>1</sup> To achieve these goals, scientists are taking a leading role in the development of this technology, which underpins general lighting and electronic displays, by customizing the emission spectrum, stability, and other properties of inorganic phosphors in the LEDs that help produce finely-tuned WL. Development of white-emitting LEDs (WLEDs) is the key step for the implementation of solid-state lighting (SSL) technologies, which are expected to address the low efficiencies of conventional incandescent and fluorescent lighting sources.<sup>2-4</sup> The present SSL technology is based on using a combination of phosphors to give the desired WL emitting devices. Three technologies are mainly used to realize solid state white lighting: first, a blue LED is coated with a yellow phosphor, giving a high luminous efficacy but poor color rendition.<sup>5,6</sup> Second, an ultraviolet LED coated with a mixture of red, green, and blue (RGB) phosphors, rendering a limited luminous efficiency as a result of the self-absorption.<sup>7,8</sup> Third, a mixture of RGB LEDs is used

directly to form a WL. However, due to the narrow spectrum of a LED device, the light formed using this method is a pseudo WL with a discontinuous spectrum.<sup>9-14</sup> Therefore, there is a growing interest in a single-component phosphor material for SSL that could overcome these short-comings.<sup>15</sup>

In this context, hybrid organic-inorganic materials (HOIMs), especially halides with perovskite-type structures, have attracted immense attention due to their remarkable structural diversity<sup>16-20</sup> and outstanding optoelectronic properties,<sup>21,22</sup> which make them promising candidates for LEDs,<sup>23-25</sup> light-emitting transistors,<sup>26</sup> laser cooling,<sup>27</sup> laser gain media,<sup>28</sup> photodetectors,<sup>29</sup> and solar cells.<sup>30,31</sup> In 2014, broadband WL emission was first reported in (110)-oriented 2D hybrid halides perovskites ( $N$ -MEDA) $PbX_4$  ( $N$ -MEDA =  $N$ 1-methylethane-1,2-diammonium)<sup>32</sup> and (EDBE) $PbX_4$  (EDBE = 2,2'-(ethylenedioxy)bis-(ethylammonium)) with  $X = Br, Cl$ ,<sup>33</sup> and in 2015 a new example of WL emission in the (100)-oriented 2D HOI perovskite ( $C_6H_{11}NH_3$ ) $PbBr_4$ .<sup>34</sup> The physical origin of the unusual WL emission was attributed to self-trapped excitons (STEs) in a deformable lattice due to the presence of strong electron-phonon coupling.<sup>32-34</sup> Follow-up studies by several research groups yielded new examples of HOIM WL emitters<sup>35-51</sup> and confirmed

their great potential in solid-state lighting applications. It was demonstrated that lowering the structural dimensionality of HOIMs enables strong quantum confinement and highly localized charges resulting in high exciton binding energies and stable excitonic emission.<sup>16, 41</sup> Among notable examples of highly luminescent HOIMs is  $C_4N_2H_{14}PbBr_4$ ,<sup>52</sup> which has a 1D crystal structure and shows an efficient bluish WL emission with photoluminescence quantum yield (PLQY) of 20% and 12% for bulk single crystals and microscale crystals, respectively.<sup>52</sup> More recently, new examples of broadband WL emitters have been reported and the specific role of the organic cation in terms of providing emissive centers has also been discussed in low dimensional HIOMs.<sup>39, 53, 54</sup> Beyond hybrid halide perovskites, Luo et al. recently reported a highly efficient and stable warm-WL emission from the all-inorganic lead-free halide double perovskites  $Cs_2(Ag_xNa_{1-x})InCl_6$  with 86% PLQY and stability over 1000 hours. Moreover, Wang et al.<sup>55</sup> reported that non-perovskite HOIMs can also have remarkable light emission properties, such as in the cases of  $(H_2DABCO)Pb_2Cl_6$  and  $(H_3O)(Et_2-DABCO)_8Pb_{21}Cl_{59}$  compounds that demonstrate WL emission with high color rendering index (CRI) values of 96 and 88, respectively. In these two materials, inorganic parts contribute to the blue emission, while the yellow/orange emission originates from the organic parts, resulting in an overall broadband WL emission.<sup>55</sup> Notably high CRI values of 96 and 88 reported for  $(H_2DABCO)Pb_2Cl_6$  and  $(H_3O)(Et_2-DABCO)_8Pb_{21}Cl_{59}$  are important; at present, the CRI of most commercial LEDs is around 80, which is considered good for use in everyday lighting.<sup>56</sup> Nonetheless, for high level color-critical applications such as museums galleries, cinematography, cosmetic sales counters, and surgery, WL emission with a CRI > 90 is desired.<sup>57</sup> The work on  $(H_2DABCO)Pb_2Cl_6$  and  $(H_3O)(Et_2-DABCO)_8Pb_{21}Cl_{59}$  confirms that non-perovskite HOIMs could also demonstrate outstanding light emission properties.<sup>55</sup> However, the development of highly-efficient broadband WL emitting HOIMs with high CRI is still in its infancy, with only a few demonstrated examples so far.

In this study, we report two new examples of HOIMs, namely  $(C_5H_7N_2)_2HgBr_4 \cdot H_2O$  (**1**) and  $(C_5H_7N_2)_2ZnBr_4$  (**2**) that demonstrate excellent light emission properties. X-ray crystallography studies suggest the presence of discrete molecular building blocks, organic  $C_5H_7N_2^+$  cations and inorganic tetrahedral  $MBr_4^{2-}$  anions, in the zero-dimensional (0D) crystal structures of  $(C_5H_7N_2)_2MBr_4$  results in strongly localized charge carriers and bright WL emission with a corresponding Commission Internationale de l'Eclairage (CIE) Color Coordinates of (0.34, 0.38) and (0.25, 0.26), and a CRI values of 87 and 96 for **1** and **2**, respectively, which are, to the best of our knowledge, among the highest values reported in the literature to date, and the highest value for Pb-free HOIMs. Metal substitution (Hg/Zn) allows us to tune the light emission from “warm” to “cold” WL with a calculated correlated color temperatures (CCT) of 5206 K for **1** and 11630 K for **2**. In addition to the record CRI values, measured room temperature PLQY values of 14.87 and 19.18% for **1** and **2**, respectively are among the highest reported for HOIMs. In particular, the 19.18% PLQY of **2** is the highest value reported for non-toxic HOIMs WL emitters to date. Our optical investigations supported by density functional theory (DFT) calculations suggested that the WL emission resulting from 4AMP-related molecular fluorescence and self-trapped state.

## EXPERIMENTAL SECTION

**Reagents used.** Chemicals listed were used as purchased and without further purification: (i) 4-aminopyridinium, 98%, Sigma; (ii) hydrobromic acid, 47% w/w, Sigma-Aldrich; (iii) zinc bromide, 99.999%, Alfa Aesar; (iv) mercury bromide, 99.9%, Fisher Scientific; (v) methanol, ACS reagent grade, Aldrich; (vi) N,N-dimethylformamide (DMF), 99%, Fisher.

**Crystal growth.** Crystals of **1** and **2** were grown through slow evaporation at room temperature under ambient conditions from stoichiometric (2:1:1 molar ratio of 4AMP to HBr to  $MBr_2$ ) methanol solutions. The 4AMP and  $MBr_2$  were solvated separately then combined and mixed for 5 mins. A stoichiometric amount of HBr was added and the solution was stirred for another 5 min and then allowed to sit at room temperature to slowly evaporate.

**Thin films preparation.** Thin films of **1** and **2** were prepared by spin coating technic. Ten milligrams of polycrystalline powder of **1** and **2** were dissolved in 1 mL of N-Ndimethylformamide (DMF) solvent and spin-coated on a quartz slide at 2500 rpm for 20 s. The film was then annealed at 80 °C for 10 min to remove residual solvent.

**Single crystal X-ray diffraction.** The X-ray intensity data for all compounds were collected on a Bruker D8 Quest Kappa-geometry diffractometer with a Photon II cpad area detector and an Incoatec Imus microfocus Mo K $\alpha$  source. The samples were cooled to 100(2) K by an Oxford Cryostream 800 LT device. All crystal structures were determined from a nonlinear least-squares fit. The data were corrected for absorption by the semi-empirical method based on equivalents and structures were solved by direct methods using the SHELXTL program and refined by full matrix least-squares on  $F^2$  by use of all reflections. All non-hydrogen atoms were refined with anisotropic displacement parameters, all occupancies were refined within two standard deviations, and all hydrogen atom positions were determined by geometry.

**Powder X-ray diffraction.** Powder X-ray diffraction (PXRD) measurements were carried out on polycrystalline powder and thin films of **1** and **2**. A Rigaku MiniFlex600 system equipped with a D/tex detector, and a Ni-filtered Cu-K $\alpha$  radiation source was used for these measurements. Scans were performed in the 3-90° (20) range, with a step size of 0.02°.

**Thermal analysis.** Simultaneous thermogravimetric analysis (TGA) and differential scanning calorimetry (DSC) measurements were carried out on a TA Instruments SDT650 unit. Measurements were done in 90  $\mu$ L alumina crucibles on 10-11 mg samples under a 100 mL/min flow of nitrogen in the 50 – 475 °C range with 5 °C/min heating rate. DSC onset temperatures were determined using TA Instrument’s TRIOS software analysis package.

**Diffuse reflectance and optical absorption.** The UV-vis diffuse reflectance measurements were measured on polycrystalline powder samples of **1** and **2**, using a PerkinElmer Lambda 750 UV/VIS/NIR Spectrometer equipped with a 100mm Spectralon InGaAs Integrating Sphere attachment over a 250-1100 nm range. The diffuse reflectance data were converted to absorption spectra according to the the Kubelka-Munk equation:<sup>58</sup>  $(F(R) = \alpha/S = (1-R)^2/(2R)$ , where R is the reflectance,  $\alpha$  is the absorption coefficient, S is the scattering coefficient. Optical absorption measurements were also performed, at room temperature, on spin-coated films of **1** and **2** and, and were deduced

from direct transmission spectra acquired using a PerkinElmer (Lambda 75) spectrophotometer.

**Photoluminescence.** Room temperature photoluminescence excitation (PLE) and PLQY measurements were performed on polycrystalline powder for **1** and **2**, and in solution for the organic 4AMP, using a HORIBA Jobin Yvon Fluorolog-3 spectrofluorometer using a Xenon lamp and Quanta- $\phi$  integrating sphere using the two-curve method in a varied range from 280–860 nm. Temperature dependence and power dependence PL measurements were done on thin films of **1** and **2**, under excitation by the 325 nm line of a HeCd laser (Kimmon Electric HeCd dual-wavelength laser, model: IK552R-F). The sample was placed on the cold finger of a helium closed-cycle cryostat and the measurements were performed from 4 to 295 K. PL decay was measured on a HORIBA Jobin Yvon Fluorolog-3 spectrofluorometer using a time-correlated-single-photon counting module. HORIBA Jobin Yvon NanoLEDs (pulsed light-emitting diodes) were used as the excitation source. The color rendering index (CRI) values were calculated using OSRAM Company's ColorCalculator software available from <https://www.osram-americas.com>.

**Computational methods.** All calculations were based on DFT implemented in the VASP code.<sup>59</sup> The interaction between ions and electrons was described by projector augmented wave method.<sup>60</sup> The kinetic energy cutoff of 400 eV for the plane-wave basis was used for all calculations. Experimental lattice parameters of **1** and **2** were used while the atomic positions were fully relaxed until the residual forces were less than 0.02 eV/Å. Electronic band structures and density of states (DOS) were calculated using Perdew–Burke–Ernzerhof (PBE) exchange-correlation functional.<sup>61</sup>

## RESULTS AND DISCUSSION

**Crystals structures and stability.** Compounds **1** and **2** crystallize in the orthorhombic space group *Pbcm* and *P2<sub>1</sub>2<sub>1</sub>2<sub>1</sub>*, respectively (see Table S1 in the Supporting Information (SI)). Interestingly, although there is no connectivity between the adjacent MX<sub>4</sub> units, both compounds exhibit pseudo-layered structures that effectively isolate the metal halide units from the organic layer, as shown in Figure 1, which is a feature found in several other group 12 metal halide systems.<sup>39, 41, 62</sup> The shortest distance between Br atoms on two adjacent MBr<sub>4</sub> units is 4.069 Å in **1** and 4.419 Å in **2**, only slightly longer than double of the bromide Shannon ionic radius (2 × r(Br<sup>−</sup>) = 3.92 Å).<sup>63</sup> Note that close-packing of halide anions can have a significant impact on the optoelectronic properties of materials. For example, whilst the vacancy-ordered double perovskites such as Rb<sub>2</sub>SnI<sub>6</sub>,<sup>64</sup> Cs<sub>2</sub>SnI<sub>6</sub><sup>64</sup> and (NH<sub>4</sub>)<sub>2</sub>PtI<sub>6</sub><sup>65</sup> have 0D crystal structures, the presence of close-packed halogen sublattice leads to the overlap of neighboring halogen *p*-orbitals providing dispersive electronic states in the vicinity of the Fermi level. Further discussions of electronic dimensionality is provided below in DFT modeling section.

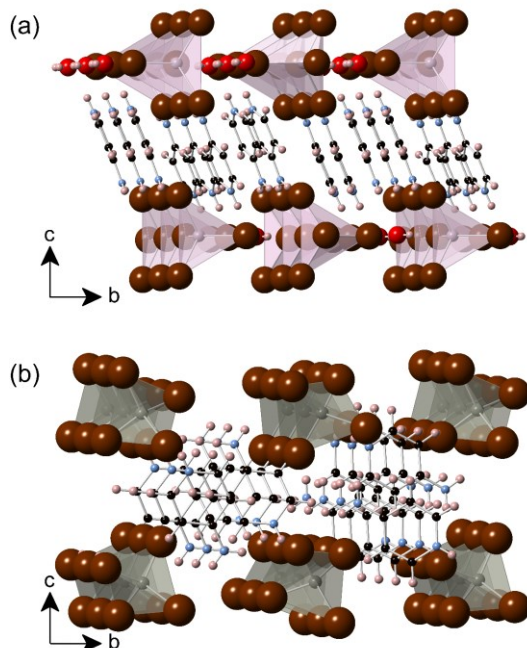


**Figure 1.** Polyhedral views of the crystal structures of (a) **1** and (b) **2**. Gray, lilac, burgundy, red, pink, blue, and black represent Zn, Hg, Br, O, H, N, and C, respectively.

Typically, 4AMP-based hybrid organic-inorganic halides of Sb and Bi are known to result in octahedral MX<sub>6</sub> units with varying connectivity such as isolated bi-octahedra in 4AMP-Bi<sub>2</sub>Cl<sub>11</sub><sup>66</sup> and 1D SbI<sub>4</sub><sup>−</sup> chains formed by edge-sharing SbI<sub>6</sub> octahedra in 4AMP-SbI<sub>4</sub>.<sup>67</sup> Interestingly, Ga,<sup>68</sup> Cd,<sup>69</sup> Cu<sup>70</sup> and Co<sup>71</sup> are also known, however, their structures are based on isolated MX<sub>4</sub> tetrahedra similar to that in **1** and **2**, whereas Pd-analog features square planar PdCl<sub>4</sub> units.<sup>72</sup> Similar to the close analogs based on Cd, (4AMP)<sub>2</sub>CdBr<sub>4</sub>·H<sub>2</sub>O<sup>69</sup> and (4AMP)<sub>2</sub>CdI<sub>4</sub>·H<sub>2</sub>O,<sup>73</sup> MX<sub>4</sub> tetrahedra in **1** and **2** are slightly distorted (presumably to optimize the hydrogen bonding network), which can be seen in the selected bond distances and angles summarized in Table S2 in the SI. In contrast, the Cu analog exhibits Jahn-Teller distorted CuCl<sub>4</sub> tetrahedra, whereas distortions in Sb- and Bi-based halides of 4AMP cation are attributed to the presence of lone pair on the metal cations.<sup>66, 67</sup>

Instability of HOIM halides is a widely known issue in literature and remains a major barrier for their industrial-scale implementation in applications such as solar cells.<sup>74–76</sup> The air and thermal stability of **1** and **2** compounds were investigated through measurements taken over a period of two months and simultaneous thermogravimetric analysis (TGA) and differential scanning calorimetry (DSC) measurements. Figure S2 shows that the sample **1** is stable in ambient air for several weeks, which is more air-stable than similar HOIMs such as (CH<sub>3</sub>NH<sub>3</sub>)<sub>2</sub>CdX<sub>4</sub> (X = Cl, Br, I).<sup>41, 62, 75</sup> However, especially for **2**, the crystallinity slightly decreases over time, and emergence of small impurity peaks are noticeable in both **1** and **2** after 1–2 months. On the other hand, TGA and DSC measurements presented in Figure S3 show the typical mass loss above 300 °C as seen in many HOIMs.<sup>77, 78</sup> Thus, as shown in Figure S3a, **1** first loses its solvated water at 110 °C (T<sub>1</sub>) and undergoes an associated structural transition at 119 °C (T<sub>2</sub>). This is followed by a

third transition at 189 °C ( $T_3$ ), attributed to melting, and evaporation of sample with onset temperature of 345 °C ( $T_4$ ). In comparison, the DSC and TGA curves of non-hydrated **2**, shown in Figure S3b, are simpler with only two thermal events at 239 and 415 °C labeled as  $T_1$  and  $T_2$ , respectively. The first event ( $T_1$ ) likely corresponds to a melting transition whereas  $T_2$  corresponds to the vaporization of the sample. Note that some of the other well-known HOIMs decompose at lower temperatures such as  $\text{CH}_3\text{NH}_3\text{PbBr}_3$  at 176 °C,  $\text{FASnPbI}_3$  (FA = formamidinium) at 150 °C, and  $\text{FASnI}_3$  at 100 °C<sup>79</sup> which suggest that **1** and **2** are relatively more thermally stable than these compounds. On the other hand, since we did the temperature dependence PL measurements on thin films of **1** and **2**, we also measured their PXRD at room temperature. The Pawley fittings of the measured PXRD data show a good matching with the calculated data based on single crystals X-ray diffraction (Figure S4).

**Optical properties.** Figure 2a shows room temperature diffuse reflectance spectra of polycrystalline powders of **1** and **2**. Sharp band edges were observed, characteristic of a direct gap semiconductor. Based on the Kubelka-Munk function ( $F(R) = \alpha/S = (1-R)^2/(2R)$ , where  $R$  is the reflectance,  $\alpha$  is the absorption coefficient,  $S$  is the scattering coefficient), band gap energies can be estimated from the Tauc plots  $[F(R)hv]^{1/\gamma}$  as a function of the photon energy ( $h\nu$ ), where  $\gamma$  is equal to 1/2 for direct transitions and 2 for indirect transitions.<sup>80</sup> This method it is often used to estimate an optical band gap of a given semiconductor with parabolic bands at the Fermi energy level. Using the direct and indirect fitting scenarios, band gaps energies of 3.44 and 4.02 eV (direct) and 3.20 and 3.90 eV (indirect) are estimated for **1** and **2** respectively (Figure S5). Although this analysis is in accordance with the literature reported procedures<sup>40-43, 81</sup> and the obtained values are reasonable, the present case is quite different due to low dimensional crystal and electronic structures of **1** and **2** compounds. Thus, **1** and **2** show an excitonic absorption features at 370 and 320 nm for **1** and **2** respectively, which may obscure the absorption onset (Figure 2a-c). Therefore, we directly measured the optical absorption spectra on spin-coated thin films of **1** and **2**. Based on the absorption spectra shown in Figure S6, we deduced a band gaps of 3.64 eV and 4.1 eV for **1** and **2**, respectively.

Under 325 nm UV irradiation, PL spectrum of **1** shows a very broad emission, Gaussian shaped, with a maximum intensity at 535 nm, a full width at half maximum (FWHM) of 233 nm, and a large Stokes-shift (~170 nm) compared to the excitonic absorption (Figure 2b). Moreover, PLE spectrum shows a sharp excitonic peak located at 370 nm in excellent agreement with the absorption spectrum peak (Figure 2b and Figure S6), attributed to excitonic absorption. Similarly, for **2**, room temperature PL spectrum shows a bright broadband emission with a maximum at 438 nm accompanied with a shoulder at 490 nm and a weaker emission band at 610 nm. Likewise, PLE spectrum of **2** shows a sharp peak at 320 nm characteristic of the excitonic absorption (Figure 2c). A large Stokes shift of 118 nm was also observed for **2**, which is often the case in 0D HOIMs.<sup>82, 83</sup> Importantly, the broadband emission of the studied compounds yield CIE Color Coordinates of (0.34, 0.38) and (0.25, 0.26), and very high CRI values of 87 and 96 for **1** and **2**, respectively (Figure 2d), which are among the highest reported in the literature to date.<sup>84</sup> It is well-known that CRI is an important parameter for WL emissive materials, reflecting the ability of a light source to accurately render the colors of an object compared to daylight. Other notable examples of WL emitting

HOIMs with high CRI values include distorted 2D corrugated hybrid perovskites such as  $\text{EA}_4\text{Pb}_3\text{Br}_{10-x}\text{Cl}_x$  (EA = ethylammonium),  $(\text{N-MEDA})\text{PbBr}_4$ ,  $(\text{N-MEDA})\text{PbBr}_4\text{Cl}_{0.5}$ , and  $(\text{DMEN})\text{PbBr}_4$  with CRI ranging from 66 to 85<sup>32, 40, 81</sup> and more recently CRI value of 93 was reported by Z. Wu et al. for the 2D corrugated (110)-oriented hybrid perovskite  $\text{N}-(3\text{-aminopropyl})\text{imidazole tetrachloroplumbate}$ .<sup>84</sup> Here, the CRI value of 96 for **2** present matches the record high CRI of  $(\text{H}_2\text{DABCO})\text{Pb}_2\text{Cl}_6$  for single-component WL emissive materials,<sup>55</sup> however, advantageously, **2** is based on a nontoxic Zn-based composition as opposed to the toxic heavy element Pb-based compound  $(\text{H}_2\text{DABCO})\text{Pb}_2\text{Cl}_6$ . On the other hand, the CIE coordinates, especially for **1**, are very close to the for white point coordinates (0.33,0.33). Furthermore, the room temperature WL PLQY of 14.87 (**1**) and 19.18% (**2**) are higher than the values reported for the lead halide perovskites.<sup>85</sup>

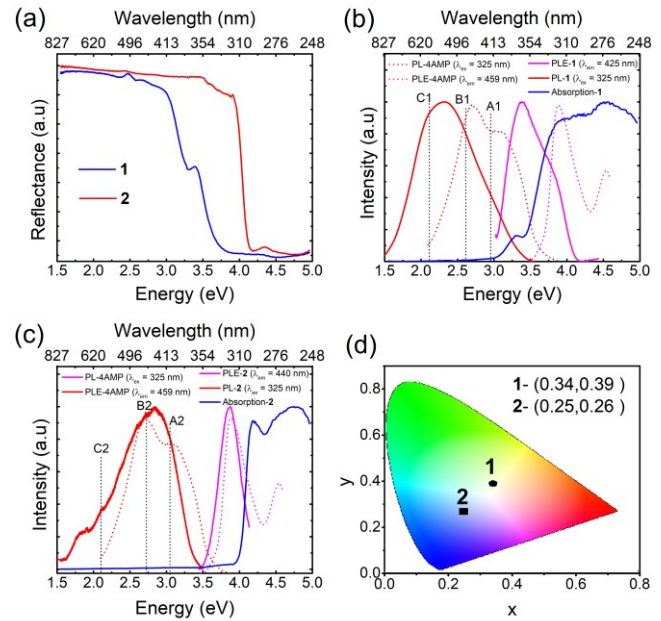


**Figure 2.** (a) Diffuse reflectance spectra of polycrystalline powders of **1** and **2** measured at room temperature. (b-c) Room temperature optical absorption (blue), PLE (pink), and PL (red) spectra of **1** and **2**, respectively. The PL and PLE spectra of the organic 4AMP are presented by red and pink dashed lines. (d) The position of **1** (circle) and **2** (square) values in the CIE 1931 chart.

Usually, the physical origin of broadband WL emission based on HOIMs is attributed to STEs in a deformable inorganic sublattice due to the presence of strong electron-phonon coupling.<sup>32-45, 48-50, 86, 87</sup> However, a few recent examples attribute the broadband emission to the coexistence of STEs PL peak on inorganic units and a fluorescence peak from emissive centers of the organic molecules, which combine to form a broadband emission covering the entire visible spectrum.<sup>39, 53-55</sup> On the other hand, our recent report on photophysical properties of some 0D HOIMs based on group 12 metals (Zn and Cd) showed that broadband emission could be the consequence of exciton localization on the aromatic organic molecular cations.<sup>62</sup> Here, to investigate the origin of the broadband emission for **1** and **2**, we measured the room temperature PL and PLE spectra of the organic salt 4AMP. As shown in Figures 2b and 2c, under 325 nm excitation, the maximum emission of 4AMP lies in the blue region with the presence of a sharp peak at 457 nm accompanied

with a shoulder at 395 nm, and PLE spectrum show a sharp peak at 325 nm. Moreover, by comparing the PL spectrum of **2** with that of the corresponding 4AMP, we observed an unmistakable and significant correspondence between the high-energy peaks near the band edge (A2 and B2) with that of the 4AMP (See Figure 2c). Likewise for **1**, the presence of a very broadband emission could be the result of the overlap of at least three emission sub-bands noted A1, B1, and C1 in Figure 2b. Importantly, the deconvolution of the room temperature PL spectrum of **1** using three Gaussian function shows a good matching between the position of the two emission bands of 4AMP and the two high energy PL bands A1 and B1 (see Figure S7). According to this, we attribute the high energy A1, B1 and A2, B2 PL bands to the 4AMP-related organic molecules emission.

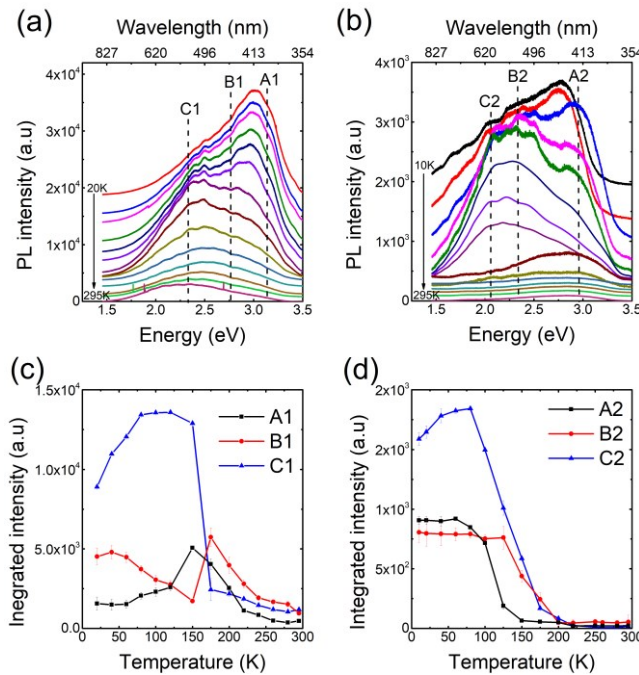


**Figure 3.** Temperature dependence PL of (a) **1** and (b) **2**, under 325 nm UV irradiation. Plots of the temperature-dependence integrated intensity of (c) A1, B1, and C1 peaks of **1** and (d) A2, B2, C2 of **2**.

Figures 3a and 3b show the temperature dependence PL measurements for **1** and **2** under 325 nm excitation. Significant changes were observed as a function of temperature for both compounds. For **1**, the room temperature broadband WL emission clearly splits into at least three sub-bands at low temperature noted as A1, B1, and C1 in Figure 3a, which are located around 400, 450 and 535 nm, respectively. Based on the deconvolution of the PL spectra using 3 Gaussian function, we deduced the thermal evolution of the integrated intensity, FWHM, and position of each PL peak of **1** and **2** (Figure 3b-c and Figure S5). Upon cooling, the integrated PL intensity of A1 first increases then decreases below 150 K. However, the integrated intensities of B1 and C1 first increases by cooling then dramatically quench bellow 150 K (Figure 3c). Similar behavior was also observed for **2** (Figure 3d) and in several HOIMs.<sup>44, 81, 85, 88</sup> Moreover, the thermal evolution of the position and the FWHM of PL peaks show an abrupt shift of the position and the width of peaks in 150-175 K temperature range. Such a critical behav-

ior was observed in several HOIMs and was attributed to structural phase transition, which could have an important impact on the optical properties.<sup>19, 22, 37</sup> However, for **1** and **2**, the possibility of the presence of structural phase transition in 150-175 K temperature range has been ruled out, as a result of the well matching of the room temperature PXRD data and the single crystal XRD data measured at 100K (see Figure S1). Thus, the PL behavior in 150-175K temperature range could be the result of a strong competition in the recombination process between the multiple emission peaks.

It is also worth noticing that the presence of permanent defect states in semiconductors could create a broadband emission.<sup>3, 82</sup> However, the concentration and recombination lifetime permanent defect are finite, thus their PL could be saturated at high excitation power.<sup>89</sup> In the case of **1** and **2** compounds, as shown in Figure S9, the intensity of C1 and C2 PL peaks present a linear dependence with excitation intensity, and the absence of saturation exclude the possibility of permanent defects emission.<sup>34, 35, 44</sup> However, the evolution of the integrated intensity of A1, B1 and A2, B2 PL peaks of **1** and **2** as a function of excitation power show a small quenching above 20 W/cm<sup>2</sup> excitation power which is probably due to the degradation of the organic molecules at high excitation intensity. (Figure S9).

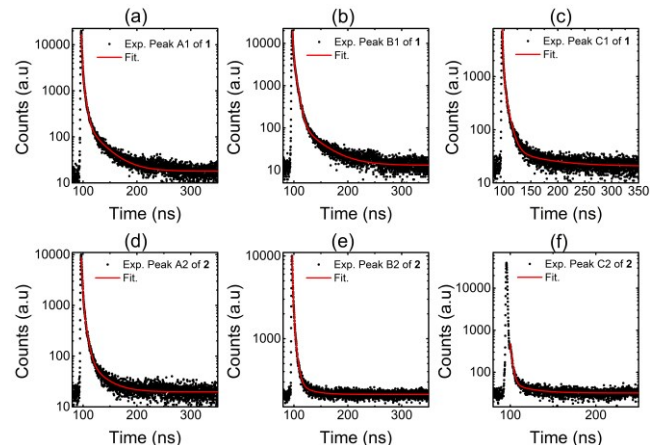


**Figure 4.** The photoluminescence decay curves of (a-c) A1, B1, and C1 PL peaks of **1** and (d-f) A2, B2, and C2 PL peaks of **2**. The excitation wavelengths are 370 and 314 nm for **1** and **2** respectively.

To understand the nature of excitons and the origin of the broadband WL emission of **1** and **2**, we measured the time-resolved PL for each PL peak (Figure 4). The excitation wavelengths used are 370 and 314 nm for **1** and **2** respectively, and the emission wavelengths are 400 (A1), 450 (B1) and 535 nm (C1) for **1**, and 438 (A2), 550 (B2), and 650 nm (C2) for **2**. All decay profiles can be fitted by a three-exponential function. The first lifetime component of 1-2 ns for all peaks of **1** and **2** is due to the instrumental response because of the duration of the light pulse (2 ns). Results show that the fast component is dominant for all PL peaks of **1** and **2** and measure  $t_2(A1) = 4.3$  ns,  $t_2(B1) = 5.1$  ns,  $t_2(C1) = 7.5$  ns,  $t_2(A2) = 5.3$  ns, and  $t_2(B2) = 4.7$  ns, and  $t_2(C2) = 2.4$  ns. As discussed above, the PL peaks of A and B are most likely due to the emission by 4AMP molecules. This is further supported by their fast decay (on the order of nanosecond) because spin-singlet excitons in aromatic molecules typically have lifetimes of nanoseconds.<sup>62</sup> However, the low-energy C1 PL band of **1** could be due to the emission of STEs

localized at  $\text{HgBr}_4$  inorganic tetrahedra (see DFT results below). The fast decay of C1 (7.5 ns) is likely the result of significant nonradiative decay. Note that the reported spin-triplet STE decay times at room temperature in Pb-based HOIMs range from a few nanoseconds to hundreds of ns.<sup>40, 52, 55, 85, 90</sup> Short STE decay times typically correlate with relatively low PLQEs (<20%)<sup>86, 52</sup> while long decay times were observed in those with

high PLQEs (>80%), indicating the strong influence of nonradiative recombination in PL decay. Concerning C2 PL band of **2**, which is dominant at low temperature (see Figure 3d) could be the result of possible inhomogeneity of organic molecules, which may significantly perturb electronic states. The attribution of the dominant PL peaks at room temperature to STEs in inorganic anions in **1** and 4AMP organic molecules in **2** is supported by band structure calculations (see below).

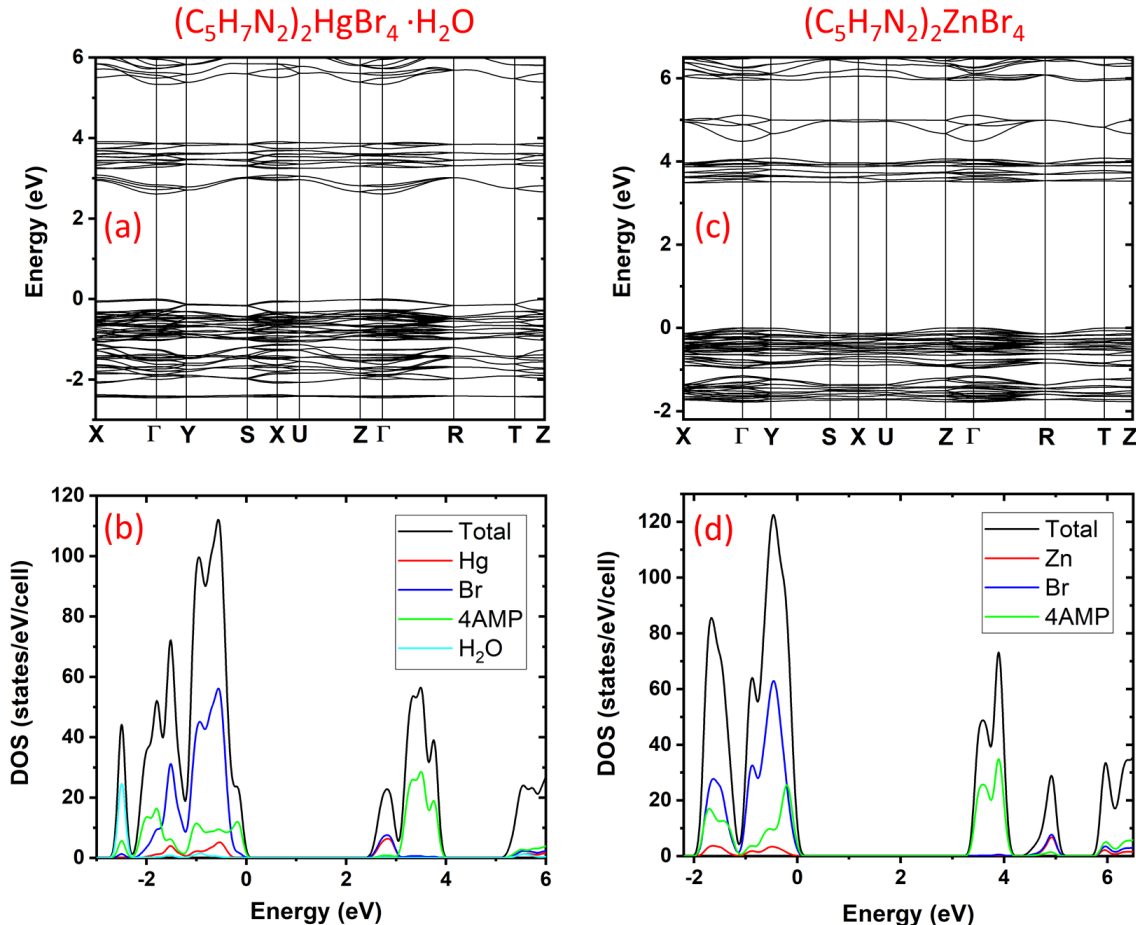


**Figure 5.** Electronic band structure and density of states (DOS) plots for **1** (a-b) and **2** (c-d) calculated using the PBE functional. Note that the band gap is underestimated due to well-known band gap error of PBE calculations.

DFT modeling. DFT-PBE calculations show that **1** has a direct band gap of 2.61 eV at the  $\Gamma$  point, and **2** has a slightly indirect band gap of 3.49 eV; the direct band gap at the  $\Gamma$  point is only 0.02 eV higher in energy. The valence band maximum (VBM) of **2** is at the  $\Gamma$  point and the conduction band minimum (CBM) is located between the X and the  $\Gamma$  points (Figure 5). Note that the above band gap values are lower than the experimentally measured values due to the well-known band-gap error in the PBE calculation. As shown in Figure 5, the conduction and valence bands of the two compounds have very small dispersion especially in the case of **2**. The conduction band of **1** (between 2.5 eV and 3.0 eV in Figure 5a) is distributed on

$\text{HgBr}_4$  clusters as shown by the partial density of states (DOS) in Figure 5b. The higher-energy flat band between 3.0 eV and 4.0 eV is made up of highly localized organic molecular orbitals. The valence band of **1** has a mixing of organic and inorganic states; however, the organic molecular states are dominant near

the VBM. A careful examination of the eigenstates reveals that the energy gap for the inorganic cluster is about 0.28 eV smaller

than that for the organic molecules. This result suggests that the lowest-energy exciton should be localized at  $\text{HgBr}_4$  clusters. The conduction band of **2** (about 3.5 eV - 4 eV in Figure 5c) is made up of highly localized organic molecular orbitals (see DOS in Figure 5d) as evidenced by the flatness of the bands. The more dispersive band above 4.5 eV with about half an eV

band width is distributed among  $\text{ZnBr}_4$  clusters. The bands near the VBM have strong character of both organic and inorganic components. The energy gap for the organic component is about 1 eV lower than that of the inorganic component. Therefore, it is expected that an exciton prefers to be localized on a 4AMP organic molecule. The experimentally measured short PL decay time indeed suggests fast singlet-exciton emission from organic molecules. Moreover, despite the two compounds have a quite similar structural coordination environment (see Figure 1), the PLQY of **2** is higher than **1**. This may be explained by the fact that the conduction band of **1** is more disperse than that of **2** (see Figure 5) which suggests that excitons in **1** may be more delocalized and more mobile than those in **2**. The larger spectral overlap between excitation and emission in **1** (Figure 2b-c) should also promote exciton migration by resonant transfer of excitation energy.<sup>91, 92</sup> More efficient exciton migration could lead to a higher probability of encountering defects, resulting in increased energy loss and lower PLQY.<sup>93</sup> Thus, the lower PLQY in **1** compared to **2** is likely due to more mobile excitons in **1**.

## CONCLUSION

In summary, we report new examples of low-dimensional HOIM for WL emission applications. The 4AMP cation configured orthorhombic 0D crystal structures feature  $\text{HgBr}_4$  and  $\text{ZnBr}_4$  isolated tetrahedra in **1** and **2**, respectively. The presence of discrete molecular building blocks in the 0D structures result in strongly localized charges and bright WL luminescence with a corresponding CIE Color Coordinates of (0.34, 0.38) and (0.25, 0.26), a very high CRI of 87 and 96, CCT values of 5206 K and 11630 K for **1** and **2**, respectively. The substitution of Hg with Zn leads to tune the emission from “warm” to “cold” WL with a calculated correlated color temperatures (CCT) of 5206 K for **1** and 11630 K for **2**. Importantly, high PLQY values of 14.87 and 19.18% were measured for **1** and **2**. Our optical investigations supported by DFT calculations suggest that the WL emission results from excitons localized in 4AMP and STEs. The observation of non-toxic (for **2**), highly efficient “cold” WL emission with a record CRI opens interesting perspectives in the design of single-component WLEDs. Therefore, we believe that this work will enrich HOIMs family with WL emission by arousing a renewed research on low cost, eco-friendly raw materials (in the case of Zn-based compound), with facile synthesis and excellent optical properties. Within this context, we anticipate that these results will stimulate research on single-emitter-based WL-emitting phosphors and diodes for next-generation lighting and display technologies to replace conventional inorganic rare-earth- and quantum dot-based phosphors that currently dominate the field of optically pumped WLEDs.

## ASSOCIATED CONTENT

### Supporting Information

The Supporting Information is available free of charge on the ACS Publications website.

Tables with single-crystals X-ray diffraction data, atomic coordinates, interatomic distances and bond angles, powder X-ray diffraction patterns, DSC/TGA, diffuse reflectance and power dependence photoluminescence data.

CCDC 1887021 and 187022 contains the supplementary crystallographic data for this paper. These data can be obtained free of

charge from The Cambridge Crystallographic Data Centre via [www.ccdc.cam.ac.uk/data\\_request/cif](http://www.ccdc.cam.ac.uk/data_request/cif).

## AUTHOR INFORMATION

### Corresponding Authors

\* (M.-H.D). E-mail [mhdu@ornl.gov](mailto:mhdu@ornl.gov)

\* (B.S). E-mail [saparov@ou.edu](mailto:saparov@ou.edu)

### Author Contributions

The manuscript was written through contributions of all authors. All authors have given approval to the final version of the manuscript. T. M. M prepared the sample, R.R performed the XRD measurements, A.Y carried out the optical measurements and wrote the paper, Y.W did the time resolved photoluminescence measurements, M-HD did the DFT calculations, and BS supervised the work. <sup>‡</sup>A.Y and R.R contributed equally.

### Notes

The authors declare no competing financial interest.

## ACKNOWLEDGMENT

We acknowledge the financial support for this work provided by the University of Oklahoma startup funds and by a grant from Oklahoma Center for the Advancement of Science and Technology (OCAST) under grant AR18-008. M.-H. Du was supported by the U. S. Department of Energy, Office of Science, Basic Energy Sciences, Materials Sciences and Engineering Division. We thank Dr. Douglas R. Powell for his help with the single crystal X-ray diffraction measurements collected on instruments purchased using NSF grants CHE-1726630.

## REFERENCES

1. Jacoby, M., Tuning phosphors for better white light. *C&En Global Entreprise* **2018**, 96, (46), 28-32.
2. Shang, M.; Li, C.; Lin, J., How to produce white light in a single-phase host? *Chem. Soc. Rev.* **2014**, 43, (5), 1372-1386.
3. Bowers, M. J.; McBride, J. R.; Rosenthal, S. J., White-Light Emission from Magic-Sized Cadmium Selenide Nanocrystals. *J. Am. Chem. Soc.* **2005**, 127, 15378.
4. Reineke, S.; Lindner, F.; Schwartz, G.; Seidler, N.; Walzer, K.; Lüssem, B.; Leo, K., White organic light-emitting diodes with fluorescent tube efficiency. *Nature* **2009**, 459, 234.
5. Yum, J.-h.; Seo, S.-Y.; Lee, S.; Sung, Y.-E.,  $\text{Y}_3\text{Al}_5\text{O}_12$ :  $\text{Ce}_0.05$  Phosphor Coatings on Gallium Nitride for White Light Emitting Diodes. *J. Electrochem. Soc.* **2003**, 150, (2), H47-H52.
6. Lee, K. H.; Lee, S. W. R. *Process development for yellow phosphor coating on blue light emitting diodes (LEDs) for white light illumination*, 8th Electronics Packaging Technology Conference, **2006**; pp 379-384.
7. Ohno, Y. In *Color rendering and luminous efficacy of white LED spectra*, 4th International

- Conference on Solid State Lighting, International Society for Optics and Photonics, **2004**, pp 88-99.
8. Speier, I.; Salsbury, M. In *Color temperature tunable white light LED system*, 6th International Conference on Solid State Lighting, 2006; International Society for Optics and Photonics: **2006**; p 63371F.
  9. Im, W. B.; George, N.; Kurzman, J.; Brinkley, S.; Mikhailovsky, A.; Hu, J.; Chmelka, B. F.; DenBaars, S. P.; Seshadri, R., Efficient and color-tunable oxyfluoride solid solution phosphors for solid-state white lighting. *Adv. Mater.* **2011**, 23, (20), 2300.
  10. Pan, M.; Du, B.-B.; Zhu, Y.-X.; Yue, M.-Q.; Wei, Z.-W.; Su, C.-Y., Highly Efficient Visible-to-NIR Luminescence of Lanthanide(III) Complexes with Zwitterionic Ligands Bearing Charge-Transfer Character: Beyond Triplet Sensitization. *Chem. Eur. J.* **2016**, 22, (7), 2440-2451.
  11. Wu, J. L.; Gundiah, G.; Cheetham, A. K., Structure–property correlations in Ce-doped garnet phosphors for use in solid state lighting. *Chem. Phys. Lett.* **2007**, 441, 250.
  12. Ye, S.; Xiao, F.; Pan, Y. X.; Ma, Y. Y.; Zhang, Q. Y., Phosphors in Phosphor-Converted White Light-Emitting Diodes: Recent Advances in Materials, Techniques and Properties. *Mater. Sci. Eng., R* **2010**, 71, 1.
  13. Stoumpos, C. C.; Kanatzidis, M. G., Halide Perovskites: Poor Man's High-Performance Semiconductors. *Adv. Mater.* **2016**, 28, (28), 5778-5793.
  14. Chen, D.; Wan, Z.; Zhou, Y.; Zhou, X.; Yu, Y.; Zhong, J.; Ding, M.; Ji, Z., Dual-Phase Glass Ceramic: Structure, Dual-Modal Luminescence, and Temperature Sensing Behaviors. *ACS Appl. Mater. Interfaces* **2015**, 7, (34), 19484-19493.
  15. Bai, X.; Caputo, G.; Hao, Z.; Freitas, V. T.; Zhang, J.; Longo, R. L.; Malta, O. L.; Ferreira, R. A. S.; Pinna, N., Efficient and tuneable photoluminescent boehmite hybrid nanoplates lacking metal activator centres for single-phase white LEDs. *Nat. Commun.* **2014**, 5, 5702.
  16. Saparov, B.; Mitzi, D. B., Organic–Inorganic Perovskites: Structural Versatility for Functional Materials Design. *Chem. Rev.* **2016**, 116, 4558-4596.
  17. Mercier, N.; Louvain, N.; Bi, W., Structural diversity and retro-crystal engineering analysis of iodometalate hybrids. *CrystEngComm* **2009**, 11, (5), 720-734.
  18. Billing, D. G.; Lemmerer, A., Inorganic–organic hybrid materials incorporating primary cyclic ammonium cations: The lead bromide and chloride series. *CrystEngComm* **2009**, 11, (8), 1549-1562.
  19. Yangui, A.; Sy, M.; Li, L.; Abid, Y.; Naumov, P.; Boukheddaden, K., Rapid and robust spatiotemporal dynamics of the first-order phase transition in crystals of the organic-inorganic perovskite  $(C_{12}H_{25}NH_3)_2PbI_4$ . *Sci. Rep.* **2015**, 5, 16634.
  20. Dammak, H.; Yangui, A.; Triki, S.; Abid, Y.; Feki, H., Structural characterization, vibrational, optical properties and DFT investigation of a new luminescent organic–inorganic material:  $(C_6H_{14}N)_3Bi_2I_9$ . *J. Lumin.* **2015**, 161, 214-220.
  21. Mitzi, D. B.; Chondroudis, K.; C.R.Kagan, Organic-inorganic electronics. *IBM J. Res. & Dev.* **2001**, 45, (1), 29-45.
  22. Yangui, A.; Pillet, S.; Garrot, D.; Triki, S.; Abid, Y.; Boukheddaden, K., Evidence and detailed study of a second-order phase transition in the  $(C_6H_{11}NH_3)_2[PbI_4]$  organic-inorganic hybrid material. *J. Appl. Phys.* **2015**, 117, (11), 115503: 1-9.
  23. Yuan, M.; Quan, L. N.; Comin, R.; Walters, G.; Sabatini, R.; Voznyy, O.; Hoogland, S.; Zhao, Y.; Beauregard, E. M.; Kanjanaboons, P.; Lu, Z.; Kim, D. H.; Sargent, E. H., Perovskite Energy Funnels for Efficient Light-Emitting Diodes. *Nat. Nanotechnol.* **2016**, 11, 872.
  24. Pan, J.; Quan, L. N.; Zhao, Y.; Peng, W.; Murali, B.; Sarmah, S. P.; Yuan, M.; Sinatra, L.; Alyami, N. M.; Liu, J.; Yassitepe, E.; Yang, Z.; Voznyy, O.; Comin, R.; Hedhili, M. N.; Mohammed, O. F.; Lu, Z. H.; Kim, D. H.; Sargent, E. H.; Bakr, O. M., Highly Efficient Perovskite-Quantum-Dot Light-Emitting Diodes by Surface Engineering. *Adv. Mater.* **2016**, 28, (39), 8718-8725.
  25. Hao, Y.; Meng, W.; Xu, H.; Wang, H.; Liu, X.; Xu, B., White organic light-emitting diodes based on a novel Zn complex with high CRI combining emission from excitons and interface-

- formed electroplex. *Org Electron.* **2011**, 12, (1), 136-142.
26. Chin, X. Y.; Cortecchia, D.; Yin, J.; Bruno, A.; Soci, C., Lead Iodide Perovskite Light-Emitting Field-Effect Transistor. *Nat. Commun.* **2015**, 6, 7383.
27. Ha, S.-T.; Shen, C.; Zhang, J.; Xiong, Q., Laser cooling of organic-inorganic lead halide perovskites. *Nat. Photonics* **2015**, 10, 115.
28. Sutherland, B. R.; Sargent, E. H., Perovskite photonic sources. *Nat. Photonics* **2016**, 10, (5), 295-302.
29. Liang, F.-X.; Liang, L.; Zhao, X.-Y.; Luo, L.-B.; Liu, Y.-H.; Tong, X.-W.; Zhang, Z.-X.; Huang, J. C. A., A Sensitive Broadband (UV-vis-NIR) Perovskite Photodetector Using Topological Insulator as Electrodes. *Adv. Opt. Mater.* **2019**, 7, 1801392.
30. Smith, I. C.; Hoke, E. T.; Solis-Ibarra, D.; McGehee, M. D.; Karunadasa, H. I., A Layered Hybrid Perovskite Solar-Cell Absorber with Enhanced Moisture Stability. *Angew. Chem.* **2014**, 126, (42), 11414-11417.
31. Zhao, B.; Bai, S.; Kim, V.; Lamboll, R.; Shivanna, R.; Auras, F.; Richter, J. M.; Yang, L.; Dai, L.; Alsari, M.; She, X.-J.; Liang, L.; Zhang, J.; Lilliu, S.; Gao, P.; Snaith, H. J.; Wang, J.; Greenham, N. C.; Friend, R. H.; Di, D., High-efficiency perovskite-polymer bulk heterostructure light-emitting diodes. *Nat. Photonics* **2018**, 12, 783-789.
32. Dohner, E. R.; Hoke, E. T.; Karunadasa, H. I., Self-Assembly of Broadband White-Light Emitters. *J. Am. Chem. Soc.* **2014**, 136, (5), 1718-1721.
33. Dohner, E. R.; Jaffe, A.; Bradshaw, L. R.; Karunadasa, H. I., Intrinsic White-Light Emission from Layered Hybrid Perovskites. *J. Am. Chem. Soc.* **2014**, 136, (38), 13154-13157.
34. Yangui, A.; Garrot, D.; Lauret, J. S.; Lusson, A.; Bouchez, G.; Deleporte, E.; Pillet, S.; Bendeif, E. E.; Castro, M.; Triki, S.; Abid, Y.; Boukheddaden, K., Optical Investigation of Broadband White-Light Emission in Self-Assembled Organic-Inorganic Perovskite  $(C_6H_{11}NH_3)_2PbBr_4$ . *J. Phys. Chem. C* **2015**, 119, (41), 23638-23647.
35. Hu, T.; Smith, M. D.; Dohner, E. R.; Sher, M.-J.; Wu, X.; Trinh, M. T.; Fisher, A.; Corbett, J.; Zhu, X. Y.; Karunadasa, H. I.; Lindenberg, A. M., Mechanism for Broadband White-Light Emission from Two-Dimensional (110) Hybrid Perovskites. *J. Phys. Chem. Lett.* **2016**, 7, (12), 2258-2263.
36. Smith, M. D.; Jaffe, A.; Dohner, E. R.; Lindenberg, A. M.; Karunadasa, H. I., Structural Origins of Broadband Emission from Layered Pb-Br Hybrid Perovskites. *Chem. Sci.* **2017**, 8, 4497-4504.
37. Yangui, A.; Pillet, S.; Mlayah, A.; Lusson, A.; Bouchez, G.; Triki, S.; Abid, Y.; Boukheddaden, K., Structural phase transition causing anomalous photoluminescence behavior in perovskite  $(C_6H_{11}NH_3)_2[PbI_4]$ . *J. Chem. Phys.* **2015**, 143, (22), 224201.
38. Yangui, A.; Pillet, S.; Lusson, A.; Bendeif, E. E.; Triki, S.; Abid, Y.; Boukheddaden, K., Control of the White-Light Emission in the Mixed Two-Dimensional Hybrid Perovskites  $(C_6H_{11}NH_3)_2[PbBr_{4-x}I_x]$ . *J. Alloys Compd.* **2017**, 699, 1122-1133.
39. Yangui, A.; Pillet, S.; Bendeif, E.-E.; Lusson, A.; Triki, S.; Abid, Y.; Boukheddaden, K., Broadband Emission in a New Two-Dimensional Cd-Based Hybrid Perovskite. *ACS Photonics* **2018**, 5, (4), 1599-1611.
40. Mao, L.; Wu, Y.; Stoumpos, C. C.; Traore, B.; Katan, C.; Even, J.; Wasielewski, M. R.; Kanatzidis, M. G., Tunable White-Light Emission in Single-Cation-Templated Three-Layered 2D Perovskites  $(CH_3CH_2NH_3)_4Pb_3Br_{10-x}Cl_x$ . *J. Am. Chem. Soc.* **2017**, 139, 11956-11963.
41. Rocanova, R.; Ming, W.; Whiteside, V. R.; McGuire, M. A.; Sellers, I. R.; Du, M. H.; Saparov, B., Synthesis, Crystal and Electronic Structures, and Optical Properties of  $(CH_3NH_3)_2CdX_4$  (X = Cl, Br, I). *Inorg. Chem.* **2017**, 56, (22), 13878-13888.
42. Zhuang, Z.; Peng, C.; Zhang, G.; Yang, H.; Yin, J.; Fei, H., Intrinsic Broadband White-Light Emission from Ultrastable, Cationic Lead Halide Layered Materials. *Angew. Chem., Int. Ed.* **2017**, 56, 14411-14416.
43. Peng, C.; Zhuang, Z.; Yang, H.; Zhang, G.; Fei, H., Ultrastable, cationic three-dimensional lead bromide frameworks that intrinsically emit broadband white-light. *Chem. Sci.* **2018**, 9, (6), 1627-1633.
44. Haris, M. P. U.; Bakthavatsalam, R.; Shaikh, S.; Kore, B. P.; Moghe, D.; Gonnade, R.

- G.; Sarma, D. D.; Kabra, D.; Kundu, J., Synthetic Control on Structure/Dimensionality and Photophysical Properties of Low Dimensional Organic Lead Bromide Perovskite. *Inorg. Chem* **2018**, 57, (21), 13443-13452.
45. Hu, H.; Morris, S. A.; Qiao, X.; Zhao, D.; Salim, T.; Chen, B.; Chia, E. E. M.; Lam, Y. M., Molecular engineering of two-dimensional hybrid perovskites with broadband emission for white light-emitting diodes. *J. Mater. Chem. C* **2018**, 6, (38), 10301-10307.
46. Krishnamurthy, S.; Kour, P.; Katre, A.; Gosavi, S.; Chakraborty, S.; Ogale, S., Cystamine-configured lead halide based 2D hybrid molecular crystals: Synthesis and photoluminescence systematics. *APL Mater.* **2018**, 6, (11), 114204.
47. Zhang, L.; Wu, L.; Wang, K.; Zou, B., Pressure-Induced Broadband Emission of 2D Organic-Inorganic Hybrid Perovskite  $(C_6H_5C_2H_4NH_3)_2PbBr_4$ . *Adv. Sci* **2019**, 6, 1801628.
48. Yu, J.; Kong, J.; Hao, W.; Guo, X.; He, H.; Leow, W. R.; Liu, Z.; Cai, P.; Qian, G.; Li, S.; Chen, X.; Chen, X., Broadband Extrinsic Self-Trapped Exciton Emission in Sn-Doped 2D Lead-Halide Perovskites. *Adv. Mater.* **2019**, 31, 1806385.
49. Ji, C.; Wang, S.; Li, L.; Sun, Z.; Hong, M.; Luo, J., The First 2D Hybrid Perovskite Ferroelectric Showing Broadband White-Light Emission with High Color Rendering Index. *Adv. Funct. Mater.* **2019**, 29, 1805038.
50. Brochard-Garnier, S.; Paris, M.; Génois, R.; Han, Q.; Liu, Y.; Massuyeau, F.; Gautier, R., Screening Approach for the Discovery of New Hybrid Perovskites with Efficient Photoemission. *Adv. Funct. Mater.* **2019**, 29, 1806728.
51. Wang, Z.; Zhang, J.-H.; Zhu, C.-Y.; Yin, S.-Y.; Pan, M., Tunable luminescence and white light emission of porphyrin-zinc coordination assemblies. *J Porphyr Phthalocyanines*. **2018**, 22, (09n10), 821-830.
52. Yuan, Z.; Zhou, C.; Tian, Y.; Shu, Y.; Messier, J.; Wang, J. C.; van de Burgt, L. J.; Kountouriotis, K.; Xin, Y.; Holt, E.; Schanze, K.; Clark, R.; Siegrist, T.; Ma, B., One-Dimensional Organic Lead Halide Perovskites with Efficient Bluish White-Light Emission. *Nat. Commun.* **2017**, 8, 14051.
53. Barkaoui, H.; Abid, H.; Yangui, A.; Triki, S.; Boukheddaden, K.; Abid, Y., Yellowish White-Light Emission Involving Resonant Energy Transfer in a New One-Dimensional Hybrid Material:  $(C_9H_{10}N_2)PbCl_4$ . *J. Phys. Chem. C* **2018**, 122, (42), 24253-24261.
54. Krishnamurthy, S.; Naphade, R.; Mir, W. J.; Gosavi, S.; Chakraborty, S.; Vaidyanathan, R.; Ogale, S., Molecular and Self-Trapped Excitonic Contributions to the Broadband Luminescence in Diamine-Based Low-Dimensional Hybrid Perovskite Systems. *Adv. Opt. Mater.* **2018**, 6, (20), 1800751.
55. Wang, G.-E.; Xu, G.; Wang, M.-S.; Cai, L.-Z.; Li, W.-H.; Guo, G.-C., Semiconductive 3-D haloplumbate framework hybrids with high color rendering index white-light emission. *Chem. Sci.* **2015**, 6, (12), 7222-7226.
56. Tsao, J. Y., Solid-state lighting: lamps, chips, and materials for tomorrow. *IEEE Circuits and Devices Magazine* **2004**, 20, (3), 28-37.
57. Rea, M. S.; Freyssinier, J. P., Color rendering: Beyond pride and prejudice. *Color Research & Application* **2010**, 35, (6), 401-409.
58. Kortüm, G.; Braun, W.; Herzog, G., Principles and Techniques of Diffuse-Reflectance Spectroscopy. *Angew. Chem. Int. Ed.* **1963**, 2, (7), 333-341.
59. Kresse, G.; Furthmüller, J., Efficiency of ab-initio total energy calculations for metals and semiconductors using a plane-wave basis set. *Comput. Mater. Sci.* **1996**, 6, (1), 15-50.
60. Kresse, G.; Joubert, D., From ultrasoft pseudopotentials to the projector augmented-wave method. *Phys. Rev. B* **1999**, 59, (3), 1758-1775.
61. Perdew, J. P.; Burke, K.; Ernzerhof, M., Generalized gradient approximation made simple. *Phys. Rev. Lett.* **1996**, 77, (18), 3865-3868.
62. Rocanova, R.; Houck, M.; Yangui, A.; Han, D.; Shi, H.; Wu, Y.; Glatzhofer, D. T.; Powell, D. R.; Chen, S.; Fourati, H.; Lusson, A.; Boukheddaden, K.; Du, M.-H.; Saparov, B., Broadband Emission in Hybrid Organic-Inorganic Halides of Group 12 Metals. *ACS Omega* **2018**, 3, (12), 18791-18802.
63. Shannon, R. D., Revised effective ionic radii and systematic studies of interatomic distances in halides and chalcogenides. *Acta Cryst. A* **1976**, 32, (5), 751-767.

64. Maughan, A. E.; Ganose, A. M.; Almaker, M. A.; Scanlon, D. O.; Neilson, J. R., Tolerance Factor and Cooperative Tilting Effects in Vacancy-Ordered Double Perovskite Halides. *Chem. Mater.* **2018**, 30, (11), 3909-3919.
65. Evans, H. A.; Fabini, D. H.; Andrews, J. L.; Koerner, M.; Preefer, M. B.; Wu, G.; Wudl, F.; Cheetham, A. K.; Seshadri, R., Hydrogen Bonding Controls the Structural Evolution in Perovskite-Related Hybrid Platinum(IV) Iodides. *Inorg. Chem.* **2018**, 57, (16), 10375-10382.
66. Khelifi, M.; Mkaouar, I.; Hlel, F.; Salah, A. B.; Zouari, R., Crystal structure and electrical properties study of 4-aminopyridinium chloridobismuthate(III)(C<sub>5</sub>N<sub>2</sub>H<sub>7</sub>)<sub>4</sub>.HBi<sub>2</sub>Cl<sub>11</sub>. *Ionics* **2010**, 16, (8), 709-715.
67. Mencel, K.; Piecha-Bisiorek, A.; Jakubas, R.; Kinzhylbalo, V.; Medycki, W., Hybrid organic-inorganic bismuth(III)-based material [4-NH<sub>2</sub>C<sub>5</sub>H<sub>4</sub>NH]<sub>7</sub>[BiCl<sub>6</sub>]<sub>2</sub>Cl. Crystal structure, dielectric properties and molecular motions of 4-aminopyridinium cations. *J. Mol. Struct.* **2019**, 1179, 297-303.
68. Szklarz, P.; Jakubas, R.; Bator, G.; Lis, T.; Kinzhylbalo, V.; Baran, J., Structural characterization, spectroscopic properties and phase transition in 4-aminopyridinium tetrachlorogallate(III): [4-NH<sub>2</sub>PyH][GaCl<sub>4</sub>]. *J. Phys. Chem. Solids* **2007**, 68, (12), 2303-2316.
69. Hatano, N.; Nakashima, M.; Horiuchi, K.; Terao, H.; Ishihara, H., Crystal Structure, NQR and DSC Studies of Tetrabromocadmates(II): [4-H<sub>2</sub>NC<sub>5</sub>H<sub>4</sub>NH]<sub>2</sub>CdBr<sub>4</sub> · H<sub>2</sub>O and [2,3,5,6-(CH<sub>3</sub>)<sub>4</sub>C<sub>4</sub>N<sub>2</sub>H<sub>2</sub>]CdBr<sub>4</sub>. *Z. Naturforsch. B Chem. Sci.* **2008**, 63b, p 1181-1186.
70. Kessentini, A.; Belhouchet, M.; Suñol, J. J.; Abid, Y.; Mhiri, T., Synthesis, structural, photoluminescence, vibrational and DFT investigation of the bis (4-aminopyridinium) tetrachloridocuprate(II) monohydrate. *J. Lumin.* **2014**, 149, 341-347.
71. Jebas, S. R.; Sinthiya, A.; Ravindran Durai Nayagam, B.; Schollmeyer, D.; Raj, S. A. C., Bis(4-aminopyridinium) tetrachloridocobaltate(II). *Acta Cryst. E* **2009**, 65, (5), m521.
72. Ivanova, B. B.; Arnaudov, M. G.; Mayer-Figge, H., Molecular spectral analysis and crystal structure of the 4-aminopyridinium tetrachloropalladate(II) complex salt. *Polyhedron* **2005**, 24, (13), 1624-1630.
73. Sun, Q.; Liao, S.; Yao, J.; Wang, J.; Fang, Q., Bis(4-aminopyridinium) tetraiodidocadmate monohydrate. *Acta Cryst. E* **2012**, 68, (9), m1160-m1161.
74. Leijtens, T.; Eperon, G. E.; Noel, N. K.; Habisreutinger, S. N.; Petrozza, A.; Snaith, H. J., Stability of Metal Halide Perovskite Solar Cells. *Adv. Energ. Mater.* **2015**, 5, (20), 1500963.
75. Dastidar, S.; Egger, D. A.; Tan, L. Z.; Cromer, S. B.; Dillon, A. D.; Liu, S.; Kronik, L.; Rappe, A. M.; Fafarman, A. T., High Chloride Doping Levels Stabilize the Perovskite Phase of Cesium Lead Iodide. *Nano Lett.* **2016**, 16, (6), 3563-3570.
76. Slavney, A. H.; Smaha, R. W.; Smith, I. C.; Jaffe, A.; Umeyama, D.; Karunadasa, H. I., Chemical Approaches to Addressing the Instability and Toxicity of Lead-Halide Perovskite Absorbers. *Inorg. Chem.* **2017**, 56, (1), 46-55.
77. Li, T.; Dunlap-Shohl, W. A.; Han, Q.; Mitzi, D. B., Melt Processing of Hybrid Organic-Inorganic Lead Iodide Layered Perovskites. *Chem. Mater.* **2017**, 29, (15), 6200-6204.
78. Kulicka, B.; Jakubas, R.; Ciunik, Z.; Bator, G.; Medycki, W.; Świergiel, J.; Baran, J., Structure, phase transitions and molecular dynamics in 4-methylpyridinium tetrachloroantimonate(III), [4-CH<sub>3</sub>C<sub>5</sub>H<sub>4</sub>NH][SbCl<sub>4</sub>]. *J. Phys. Chem. Solids* **2004**, 65, (5), 871-879.
79. Leijtens, T.; Prasanna, R.; Gold-Parker, A.; Toney, M. F.; McGehee, M. D., Mechanism of Tin Oxidation and Stabilization by Lead Substitution in Tin Halide Perovskites. *ACS Energy Lett.* **2017**, 2, (9), 2159-2165.
80. Tauc, J.; Grigorovici, R.; Vancu, A., Optical Properties and Electronic Structure of Amorphous Germanium. *phys. status solidi (b)* **1966**, 15, (2), 627-637.
81. Mao, L.; Wu, Y.; Stoumpos, C. C.; Wasieleski, M. R.; Kanatzidis, M. G., White-Light Emission and Structural Distortion in New Corrugated Two-Dimensional Lead Bromide Perovskites. *J. Am. Chem. Soc.* **2017**, 139, 5210.
82. Zhou, C.; Tian, Y.; Wang, M.; Rose, A.; Besara, T.; Doyle, N. K.; Yuan, Z.; Wang, J. C.; Clark, R.; Hu, Y.; Siegrist, T.; Lin, S.; Ma, B.,

- Low-Dimensional Organic Tin Bromide Perovskites and Their Photoinduced Structural Transformation. *Angew. Chem. Int. Ed.* **2017**, *56*, (31), 9018-9022.
83. Zhou, C.; Tian, Y.; Yuan, Z.; Lin, H.; Chen, B.; Clark, R.; Dilbeck, T.; Zhou, Y.; Hurley, J.; Neu, J.; Besara, T.; Siegrist, T.; Djurovich, P.; Ma, B., Highly Efficient Broadband Yellow Phosphor Based on Zero-Dimensional Tin Mixed-Halide Perovskite. *ACS Applied Materials & Interfaces* **2017**, *9*, (51), 44579-44583.
84. Wu, Z.; Ji, C.; sun, z.; Wang, S.; Zhao, S.; Zhang, W.; li, l.; Luo, J., Broadband white-light emission with high color rendering index in a two-dimensional organic-inorganic hybrid perovskite. *J. Mater. Chem. C* **2018**, *6*, (5), 1171-1175.
85. Smith, M. D.; Karunadasa, H. I., White-Light Emission from Layered Halide Perovskites. *Acc. Chem. Res.* **2018**, *51*, (3), 619-627.
86. Yuan, Z.; Zhou, C.; Messier, J.; Tian, Y.; Shu, Y.; Wang, J.; Xin, Y.; Ma, B., A Microscale Perovskite as Single Component Broadband Phosphor for Downconversion White-Light-Emitting Devices. *Adv. Opt. Mater.* **2016**, *4*, (12), 2009-2015.
87. Tiguntseva, E. Y.; Sadrieva, Z.; Stroganov, B. V.; Kapitonov, Y. V.; Komissarenko, F.; Haroldson, R.; Balachandran, B.; Hu, W.; Gu, Q.; Zakhidov, A. A.; Bogdanov, A.; Makarov, S. V., Enhanced temperature-tunable narrow-band photoluminescence from resonant perovskite nanograting. *Appl. Surf. Sci.* **2019**, *473*, 419-424.
88. Thirumal, K.; Chong, W. K.; Xie, W.; Ganguly, R.; Muduli, S. K.; Sherburne, M.; Asta, M.; Mhaisalkar, S.; Sum, T. C.; Soo, H. S.; Mathews, N., Morphology-Independent Stable White-Light Emission from Self-Assembled Two-Dimensional Perovskites Driven by Strong Exciton-Phonon Coupling to the Organic Framework. *Chem. Mater.* **2017**, *29*, 3947-3953.
89. Reshchikov, M. A.; Morkoç, H., Luminescence properties of defects in GaN. *J. Appl. Phys.* **2005**, *97*, (6), 061301.
90. Zhou, C.; Lin, H.; Worku, M.; Neu, J.; Zhou, Y.; Tian, Y.; Lee, S.; Djurovich, P.; Siegrist, T.; Ma, B., Blue Emitting Single Crystalline Assembly of Metal Halide Clusters. *J. Am. Chem. Soc.* **2018**, *140*, (41), 13181-13184.
91. Blasse, G.; Grabmaier, B. C., *Luminescent Materials*. Springer-Verlag, Berlin Heidelberg, **1994**.
92. Dexter, D. L., A Theory of Sensitized Luminescence in Solids. *J. Chem. Phys.* **1953**, *21*, (5), 836-850.
93. Han, D.; Shi, H.; Ming, W.; Zhou, C.; Ma, B.; Saparov, B.; Ma, Y.-Z.; Chen, S.; Du, M.-H., Unraveling luminescence mechanisms in zero-dimensional halide perovskites. *J. Mater. Chem. C* **2018**, *6*, (24), 6398-6405.

---

SYNOPSIS TOC: New 0D organic-inorganic hybrid materials showing a bright WL luminescence with a high PLQY of 14.87 and 19.18% and a record color rendering index (CRI) of 87 and 96.

